Navigating the landscape of nonlinear mechanical metamaterials for advanced programmability

Eder Medina, Patrick E. Farrell, Katia Bertoldi, and Chris H. Rycroft

Navigating the landscape of nonlinear mechanical metamaterials for advanced programmability

Eder Medina,[1] Patrick E. Farrell,[2] Katia Bertoldi,[1, 3] and Chris H. Rycroft[1, 4]

[1]*Harvard John A. Paulson School of Engineering and Applied Sciences, Harvard University, Cambridge, MA 02138, USA*
[2]*Mathematical Institute, University of Oxford, Oxford OX2 6GG, United Kingdom*
[3]*Kavli Institute, Harvard University, Cambridge, MA 02138, USA*
[4]*Computational Research Division, Lawrence Berkeley Laboratory, Berkeley, CA 94720, USA*[*]
(Dated: January 10, 2020)

We consider a flexible mechanical metamaterial comprising an elastomeric matrix with an embedded square array of circular holes. First, we use the deflated continuation technique of bifurcation analysis to explore its complex energy landscape, characterized by multiple bifurcations from which stable and unstable branches emanate. We then investigate how this landscape can be used to design materials with advanced programmability. We find that the response of the system can be constantly reprogrammed through local manipulation, moving it from one stable branch to another and that small targeted imperfections can be harnessed to enhance such programmability.

INTRODUCTION

Mechanical metamaterials—man-made structures with mechanical properties governed by their geometry rather than composition—are receiving increasing interest [1–3] not only because of their rich physics, but also for their unique mechanical properties, including negative Poisson's ratio [4], negative thermal expansion [5], and negative dynamic moduli [6, 7]. Intriguingly, it has been also shown that nonlinearities and instabilities can be exploited to further enhance their functionalities [3] and enable the design of systems with switchable properties [8–10] and programmable responses [11–14]. It is no surprise that such flexible systems usually have an intricate energy landscape with a plethora of energy minima [15, 16]. However, their behavior is typically studied using analyses that capture only a single solution [8–10, 13], thus limiting the range of achievable deformation-induced functionalities.

In parallel, continuation and bifurcation analysis techniques, such as simplicial continuation [17], pseudo-arclength continuation [18, 19], and branch switching [20], have emerged as powerful tools to obtain insight into the energy landscapes of physical systems. By numerically following the equilibrium equations as a function of a control parameter (e.g. a mechanical or geometrical variable of the problem), these methods enable the computation of additional equilibrium solution branches. While such techniques have been widely used to get a better understanding of numerous physical systems [21–24], their adoption in the design of mechanical metamaterials has been limited [15, 16, 25].

Here we demonstrate how a novel bifurcation analysis technique in conjunction with the rich energy landscape of flexible mechanical metamaterials can facilitate the realization of systems with advanced programmability. We consider a flexible and porous metamaterial and start by making use of a deflated continuation algorithm to identify solutions, taking advantage of the ability of this algorithm to automatically find disconnected solution branches. Then, we investigate the implications of these numerical analyses on the responses of physical samples. Remarkably, we find that the information encoded in the bifurcation diagrams can be harnessed to realize mechanical metamaterials whose responses can be reconfigured by identifying nearby stable branches and develop a deeper understanding in the interplay between small targeted imperfections and the evolution of branch connectivity which can enable advanced programmability.

NUMERICAL METHODS

We use the open-source finite-element solver FEniCS [26] to numerically investigate the nonlinear response of flexible porous structures made of a elastomeric material whose response is capture using a Neo-Hookean model with strain energy density function

$$\psi(\mathbf{F}) = \frac{\mu}{2}(I_c - 2) - \mu \ln J + \frac{\mu \nu}{1 - 2\nu}(\ln J)^2 \qquad (1)$$

where μ is the initial shear modulus, and ν being the Poisson's ratio. Moreover, $\mathbf{F} = \mathbf{I} + \nabla \mathbf{u}$ is the deformation gradient tensor (with $\mathbf{u}$ being the displacement field to be computed and $\mathbf{I}$ denoting the identity matrix) and $I_c = \mathrm{tr}\mathbf{F}^\mathsf{T}\mathbf{F}$ and $J = \det \mathbf{F}$. In all of our analysis we use plane strain conditions and discretize the models with piecewise quadratic triangular finite elements. This results in a parameterized nonlinear system of equations

$$\mathbf{R}(\mathbf{u}, \varepsilon_a) = \mathbf{0}, \qquad (2)$$

which we solve using the Newton–Raphson method to obtain a displacement field, $\mathbf{u}$, at a given applied strain, ε_a. Numerical continuation is employed to trace out the full branch as function of the applied strain.

Deflated Continuation

Standard finite element analysis and continuation techniques are only capable of capturing a single solution, reducing the opportunity for programmability. To overcome this limitation, we couple FEniCS with a deflated continuation package DEFCON [27] which enables the identification of additional

branches. The key idea of deflation is to modify Eq. (2), and remove known solutions such that the Newton–Raphson method is able to converge to a previously unknown solution. This is analogous to removing a root $x = r$ of a polynomial $p(x)$ by constructing $q(x) = p(x)/(x-r)$. In this work, the deflated problem is constructed as

$$\mathbf{G}(\mathbf{u}, \varepsilon_a; \mathbf{u}^*) = \left(\frac{1}{\|\mathbf{u} - \mathbf{u}^*\|_{H^1}^2} + 1 \right) \mathbf{R}(\mathbf{u}, \varepsilon_a) = \mathbf{0} \quad (3)$$

where $\| \cdot \|$ denotes the H^1 norm $(\| \cdot \|_{H^1}^2 = \int(\cdot)^2 d\Omega + \int(\nabla\cdot)^2 d\Omega)$ and $\mathbf{u}^*$ is an additional solution. We solve this deflated problem using the same computational techniques as for the undeflated one. Since the deflation operator removes the original solution $\mathbf{u}$ from $\mathbf{R}$ [28], if the Newton–Raphson method converges it will converge to a different solution. We iteratively apply this procedure to obtain as many solutions $\mathbf{u}^*$ as possible at a given ε_a through pre-multiplication on the augmented systems [27].

In this work, we start from $\varepsilon_a = 0$ and examine the structure in compression, taking small negative steps in ε_a. Once a solution has been successfully deflated at a given ε_a additional branches are then further traced out. Let ε_a^+ and ε_a^- denote the previous and next values of ε_a, respectively. After all known branches have been continued, all solutions at ε_a^- are deflated and each solution at ε_a^+ used as initial guess for the application of Newton–Raphson to the deflated problem. This robustly discovers new solutions introduced at connected bifurcations between $(\varepsilon_a^-, \varepsilon_a^+)$. In addition, deflation can discover disconnected branches, provided the distance between the known and disconnected branch is not too large. Such disconnected branches typically arise from symmetry-breaking perturbations that unfold connected bifurcations; they are important for understanding the behaviour of physical systems, but are generally quite difficult to discover numerically.

Stability

Having discovered a set of solution pairs $(\mathbf{u}, \varepsilon_a)$, we then determine their stability by investigating the propagation of small-amplitude oscillatory modes

$$\mathbf{W}(\mathbf{x}_0, t) = \mathbf{w}(\mathbf{x}_0)e^{-i\omega t} \quad (4)$$

superimposed upon a given state of finite deformation defined by $\mathbf{u}$, ω being the oscillation frequency and $\mathbf{x}_0$ denoting the position of a material point in the undeformed configuration. More specifically, we consider the incremental version of the equations of motion in the reference undeformed configuration [29]

$$\text{Div}\,\dot{\mathbf{S}} = \rho \frac{D^2\mathbf{W}}{Dt^2}, \quad (5)$$

where ρ is the material density and Div denotes the div operator in the reference configuration and $\frac{D}{Dt}$ is the Lagrangian time

derivative. Moreover, $\dot{\mathbf{S}}$ is the increment of total first Piola–Kirchhoff stress, which can be written as

$$\dot{\mathbf{S}} = \mathbb{L} : \dot{\mathbf{F}} \quad (6)$$

with

$$\mathbb{L}_{ijkl} = \frac{\partial^2 \psi}{\partial F_{ij} \partial F_{kl}}, \quad (7)$$

and

$$\dot{\mathbf{F}} = \frac{\partial \mathbf{W}}{\partial \mathbf{x}_0}, \quad (8)$$

where ψ is the strain energy density and $\mathbf{F}$ is the deformation gradient. Substitution of Eq. (4) into Eqs. (6) and (5) yields

$$\dot{\mathbf{S}}(\mathbf{x}_0, t) = \mathbb{L} : \frac{d\mathbf{w}(\mathbf{x}_0)}{d\mathbf{x}_0} e^{-i\omega t} \quad (9)$$

and

$$\text{Div}\left(\mathbb{L} : \frac{d\mathbf{w}(\mathbf{x}_0)}{d\mathbf{x}_0} \right) + \rho\,\omega^2 \mathbf{w} = \mathbf{0}, \quad (10)$$

which when discretized using the finite-element approach becomes

$$\left(\mathbf{K}(\mathbf{u}) + \omega^2 \mathbf{M} \right) \mathbf{w} = \mathbf{0} \quad (11)$$

where $\mathbf{K}$ is the tangent stiffness matrix, $\mathbf{M}$ is the standard mass matrix. We introduce a normalization parameter,

$$\lambda = \frac{\rho L^2}{\mu} \omega^2. \quad (12)$$

with L being the length of the structure. A positive λ corresponds to a vibration of finite amplitude, and a negative λ identifies a perturbation growing exponentially with time. Therefore, the deformed configuration defined by $\mathbf{u}$ is stable for $\lambda_{\min} \equiv \min(\lambda) > 0$ and unstable for $\lambda_{\min} < 0$.

RESULTS

We focus on structures consisting of an elastomeric matrix with an embedded square array of circular holes; a relatively simple architecture that is capable of giving rise to a rich complex energy landscape [8, 16, 25, 30, 31]. The holes have radius r and center-to-center distance a, chosen so that the initial porosity is $\psi_0 = \pi r^2/a^2 = 0.6$. Two different finite size structures are considered: one with a 2×2 array of holes and another with a 3×3 array of holes. All structures have the two vertical edges flanked by a column of semicircles and the horizontal ones ending with a strip of solid material of width a. They are made of an elastomeric material, whose response is captured by a quasi-incompressible neo-Hookean model with initial shear modulus $\mu = 49$ kPa and Poisson's ratio $\nu = 0.48$.
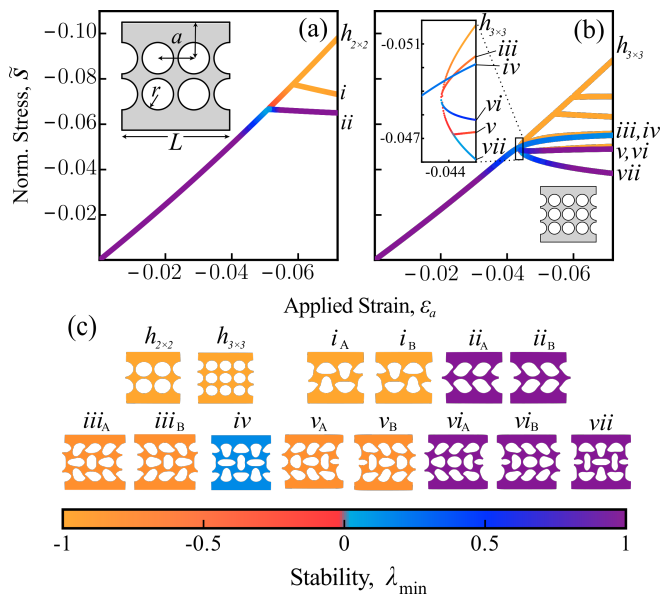
FIG. 1. (a,b) Computed bifurcation diagrams for structures with an array of (a) 2×2 and (b) 3×3 holes. The color of the branches corresponds to the minimal eigenvalue $\lambda_{\min}$, a measure of stability. The inset gray diagrams show the undeformed structures. The inset on panel (b) shows a zoomed-in region near the bifurcation. (c) Solutions corresponding to the labeled branches $h_{2\times2}$, $h_{3\times3}$, and i–vii at $\varepsilon_a = -0.07$. Collections of branches are labeled based on having an identical mechanical response, and are sub-labeled with capital letters to differentiate between left and right symmetries.

Bifurcation Analysis

In Figs. 1(a) and 1(b) we report the evolution of the normalized nominal stress, $\tilde{S} = S_{22}/\mu$, as a function of the applied strain, ε_a, for the 2×2 and 3×3 structures, respectively. As expected, we find that the response of both systems is characterized by multiple branches, some of which are stable and some unstable. Moreover, as previously observed for porous structures of small size [15, 32], our results also indicate that boundary effects present in finite-sized structures play an important role, as the bifurcation diagrams of the 2×2 and 3×3 structures are significantly different. For the considered range of applied strain, the response of the 2×2 structure is characterized by two pitchfork bifurcations. The first one at $\varepsilon_a \approx -0.051$ gives rise to a stable *sheared* post-buckled solution with all holes sheared either leftwards or rightwards, whereas from the second one at $\varepsilon_a \approx -0.058$ an unstable branch emanates, corresponding to a *polarized* configuration in which the holes alternately take horizontally and vertically dominant shapes.

The bifurcation diagram of the 3×3 structure is more intricate and, in addition to multiple unstable branches stemming from bifurcations off the main branch, contains a bifurcation point at $\varepsilon_a \approx -0.043$ from which three stable branches appear to emanate. Closer inspection shows that this bifurcation does not occur at a single point (Fig. 1(b), inset), but consists of a series of disconnected transcritical bifurcations similar to those previously observed in holey columns [15] (for transcritical

branch classification analysis see supplemental information Figs. S4–5 [33]). Moreover, we find that for the 3×3 structure both the *sheared* and *polarized* modes are stable. However, while the two symmetric *sheared* solutions share the same stress–strain curve (i.e. branches vi_A and vi_B in Fig. 1(b)), the two supported *polarized* solutions are associated to two distinct branches: the one where the central hole is vertically oriented with branch iv (which is connected to the main branch, but is only marginally stable), and the one where the central hole is horizontally oriented with branch vii. Having identified multiple solution branches under uniaxial compression, in the remainder of this paper we investigate how this energy landscape can be exploited.

Experiments

Next, we focus on the implications of the bifurcation diagrams on the response of physical samples fabricated using a molding approach out of a silicone rubber (Elite Double 8, Zhermack). We fabricate several 2×2 and 3×3 structures using different molds and then characterize their response under uniaxial compression. As shown in Fig. 2(a), we find that for all 2×2 samples the *sheared* mode emerges upon compression beyond the buckling point. Differently, none of 3×3 structures deform according to the fully connected branch (i.e. branch iv), which a standard finite-element simulation would follow (Fig. S2). Instead, they all deform according to either branches $vi_\mathrm{A,B}$ or vii (Fig. 2(b)). We attribute this to immeasurable small imperfections introduced during fabrication that cause changes to the symmetry group of the system and, ultimately, to the branch connectivity [34]. However, it is important to note that, though disconnected, other stable branches should still exist under such small imperfections. To probe their existence, we compress a sample up to a switching strain ε_S past the critical buckling point, locally manipulate its free boundary to move it onto another branch, and then further compress it. As shown in Fig. 2(c), we find that the 2×2 samples can be always moved to the other symmetric *sheared* mode. Such reconfiguration only leads to a change in geometry, since the two branches are characterized by an identical stress–strain curve. Differently, for the 3×3 structures we find that not all initially predicted stable branches can be accessed *directly* nor can they be accessed by locally manipulating the samples at the chosen ε_s. Specifically, samples that deform following branch vii can only be reconfigured to the *polarized* mode associated to branch iv (Fig. 2(d)), whereas those that follow branches $vi_\mathrm{A,B}$ can only be reconfigured to branch vii (Fig. 2(e)). Since these three branches are characterized by different stress–strain curves, branch switches are also accompanied by a change in stiffness and load bearing capacity. Note that, since the system is purely elastic, such branch switches are reversible and repeatable (Movie S2 [33]), suggesting that the response of our mechanical metamaterial can be easily reprogrammed at any time by taking it from one stable branch to another.
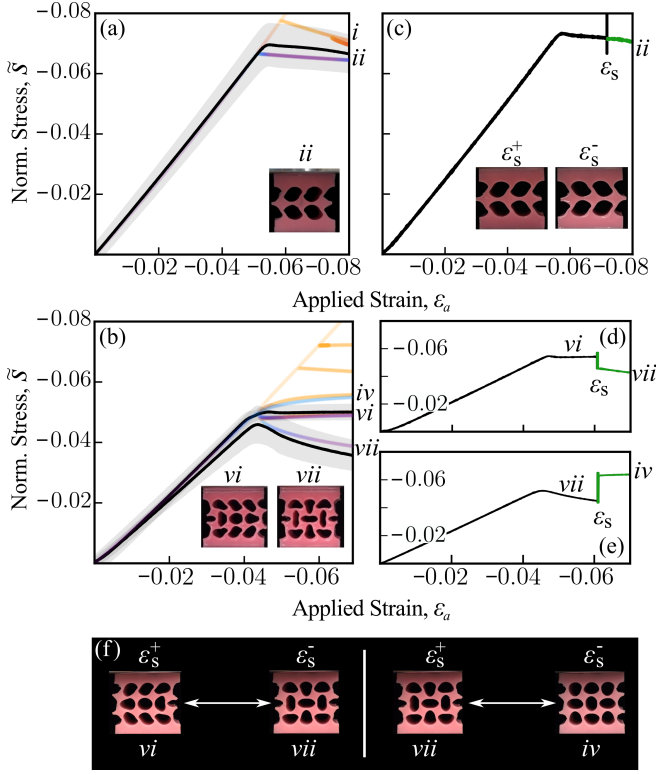
FIG. 2. (a) Experimentally measured stress–strain curve for the 2×2 structure, overlaid on the numerical bifurcation diagram from Fig. 1(a) (colored lines). The solid black line shows the average response for 4 samples, and the gray envelope shows the standard deviation. The inset shows a deformed sample at $\varepsilon_a = -0.07$, in the *sheared* ii_A mode. (b) Experimentally measured stress–strain curves for the 3×3 structure. In 10 samples tested, 7 follow branch vi and 3 follow branch vii; the averages and standard deviations for each set are plotted separately. The insets show deformed samples in both deformation modes at $\varepsilon_a = -0.07$. (c) Stress–strain curve for a single 2×2 structure that is manually switched from branch ii_A to ii_B at $\varepsilon_S = -0.072$. The curve after the switch is shown in green. Insets show the structure before (ε_S^+) and after (ε_S^-) the switch. (d,e) Stress–strain curves for two differing 3×3 structures that are manually switched from one branch to another at $\varepsilon_S = -0.06$. (f) Images of the 3×3 structures before and after the switches.

Imperfection Analysis

The results of Fig. 2 indicate that the information encoded in the bifurcation diagram can be used to program the response of the metamaterials on the fly. However, they also show that not all stable branches can be accessed, limiting the available range of programmability. To gain a better understanding of the reasons behind this limitation, we proceed by constructing the bifurcation diagrams for structures with initial mode-derived perturbations. Towards this end, we apply to the undeformed structures a perturbation field $\mathbf{u}_{\text{pert}}$ defined as

$$\mathbf{u}_{\text{pert}} = \delta \frac{\mathbf{u}_{\text{branch}} - \mathbf{u}_{h_{i \times i}}}{\|\mathbf{u}_{\text{branch}} - \mathbf{u}_{h_{i \times i}}\|_{L^2}} \tag{13}$$

where δ is the imperfection magnitude and $\mathbf{u}_{\text{branch}}$ and $\mathbf{u}_{h_{i \times i}}$ (with $i = 2, 3$) are the displacement fields at $\varepsilon_a = -0.07$ associated to the branch of interest and the $h_{i \times i}$ branch (Fig. 1), respectively. In Fig. 3 we present the bifurcation diagrams obtained for different mode-derived imperfections for $\delta = 5 \times 10^{-4}$ (top row) and $\delta = 2 \times 10^{-3}$ (bottom row). To understand our experimental results better, we focus first on Figs. 3(a), (c) and (e), where we consider small perturbations with the form of the modes that emerge during our experiments (i.e. the modes associated to branches ii_A, vi_A, and vii). For all three cases we find that the complex energy landscape of our structures is preserved, though modified. More specifically, for the 2×2 structure the ii_A-perturbation (i.e. an imperfection based on the ii_A branch) separates the *sheared* modes, but preserves both of them (Fig. 3(a)), allowing for the system to be easily reconfigured from one to the other (Fig. 2(c)). Differently, for the 3×3 structure the considered imperfections not only alter the connectivity of the branches, but also suppress some of them. In particular, the vi_A-perturbation eliminates the response associated to branch iv (Fig. 3(c)), while the vii-perturbation suppresses that associated to branch vi (Fig. 3(e)). Note that these results support the response observed in our experiments (compare Figs. 2(d,e)) and suggest that the immeasurable small imperfections introduced during fabrication have suppressed branches, which, therefore, cannot be attained through manual reconfiguration at the specified switching strain ε_S. Finally, we find that by slightly increasing δ to 2×10^{-3} (which changes the hole areas by less than 1%) the intricate bifurcating structure completely vanishes and a single smoothly-varying curve emerges. As previously observed [35, 36], these results confirm that the introduction of sizeable buckling mode-derived imperfections make the metamaterial robustly follow the targeted deformation path. However, by suppressing all other branches such imperfections limit the response of the system to only one specific mode and prevent any type of switchability.

Next, we analyze the effects of a perturbation based on branch iv, a stable branch that is never followed in our experimental tests. As shown in Fig. 3(g), we find that for this perturbation, branch iv is stable and fully connected, all other stable branches still exist and the transcritical bifurcations remain though their location is shifted above the main connected branch (Fig. 3(g), inset). As such, we expect a sample with an iv-perturbation will follow branch iv upon loading and will offer the largest set of programmable properties, since it can be switched to both branches vi and vii. This is confirmed by the experimental results in Fig. 4(a) for a sample realized using a mold designed to introduce a iv-perturbation with $\delta = 5 \times 10^{-4}$. In all our tests the sample initially deforms following branch iv, and at strain $\varepsilon_S = -0.06$ can be locally manipulated to switch to either branches vi or vii, thus supporting three responses that can be continuously accessed.
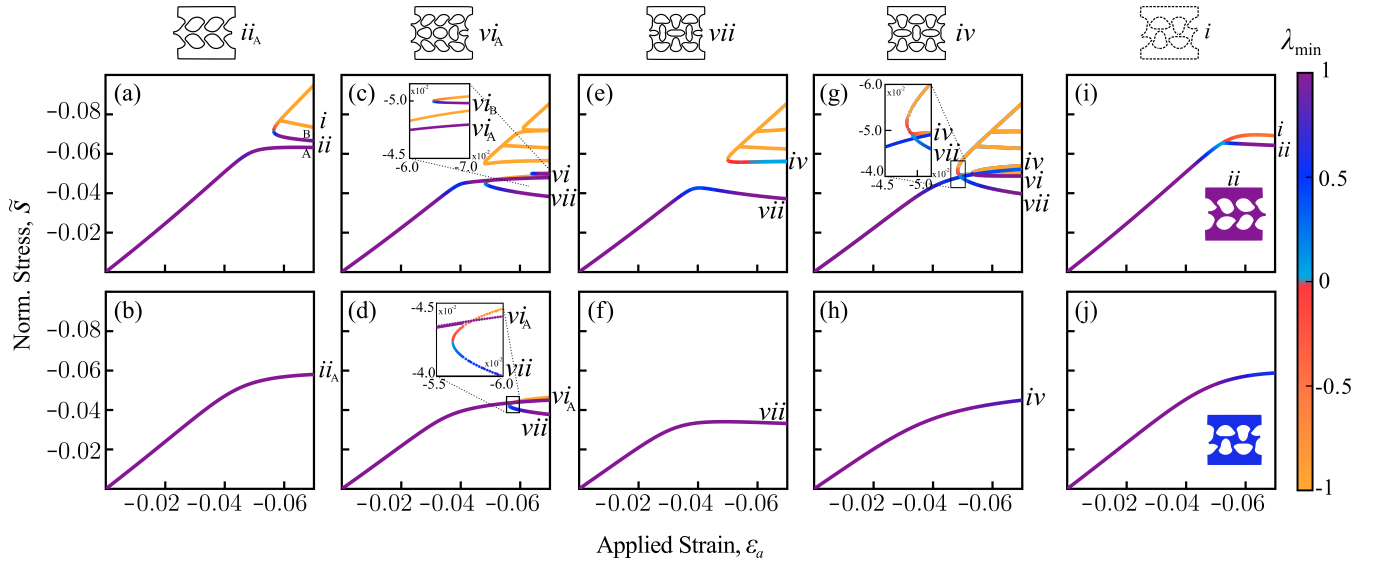
FIG. 3. Bifurcation diagrams for the perturbed structures using imperfection magnitudes of $\delta = 5 \times 10^{-4}$ (top row) and $\delta = 2 \times 10^{-3}$ (bottom row). The branches are colored according to the stability measure $\lambda_{\min}$. The five columns correspond to perturbations based on the structures from branches i_A, iv_C, v, iii, i in Fig. 1, which are plotted at the top of each column; the first four columns use perturbations based on stable branches, and the last column uses a perturbation based on an unstable branch. The images in panels (i) and (j) show the deformed structures at the end of two branches at $\varepsilon_a = -0.07$.

Branch Stabilization

Lastly, we investigate the response of the 2×2 structure with an imperfection based on the unstable branch i (Figs. 3(i) and (j)). In this case we find that for $\delta = 5 \times 10^{-4}$ branch i remains unstable and that the $h_{2\times2}$ branch vanishes, hence the system can only deform following the stable *sheared* mode. To realize the desired *polarized* mode, the magnitude of the imperfection has to be increased to $\delta = 2 \times 10^{-3}$, but this change the architecture of the structure and, therefore, significantly affects its stress–strain response, which loses the sharp transition associated to the instability. As we are limited in our ability to achieve the desired response of the unstable modes through targeted imperfection and manual reconfiguration, we therefore turn to imposing additional constraints on our original system and explore their effects on the bifurcation diagram. To suppress the stable *sheared* mode, we place a pin in the center point of the sample (Fig. 4(b), inset, top left) and guide it along a vertical trajectory. In Fig. 4(b) we show both the bifurcation diagram for the constrained structure as well as the experimentally measured stress–strain curve. Two key features emerge. First, the *sheared* branch is suppressed and, second, the *polarized* branch is stabilized. Moreover, the constraint does not affect the mechanical properties of branch i, preserving key features such as negative stiffness and a sharp buckling transition.
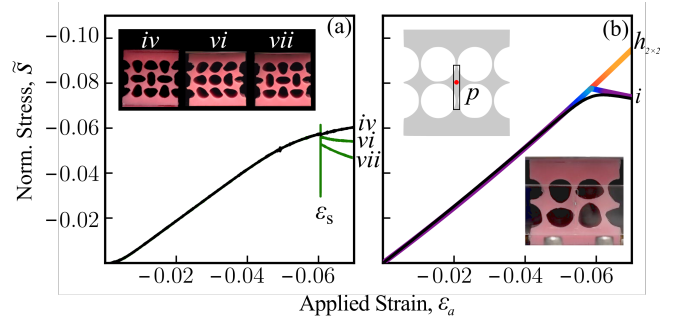

FIG. 4. (a) Experimental stress–strain curve (black) for the 3×3 structure with an *iv* perturbation. For any applied ε_a pass the bifurcation point, all three previously predicted stable branches are realizable via manual switching. The stress–strain curves after switching are shown in green and includes the noise introduced during the switching process (green vertical line). The inset images show the sample in the three different stable branches. (b) Bifurcation diagram for a 2×2 structure with its central point (red dot) constrained to move vertically. Colored lines show the simulation results using the same color scheme as in Fig. 1. The solid line shows the experimental stress–strain curve, with the experimental snapshot showing the resulting *polarized* mode. All experimental images are captured at $\varepsilon_a = -0.07$.

DISCUSSION AND CONCLUSION

In summary, we have shown that the deflated continuation technique can be used to explore the complex energy landscapes of flexible mechanical metamaterials and provide insight in the design of multistable systems with advanced functionalities. More specifically, we used the numerically obtained bifurcation diagrams to design a metamaterial whose mechan-

ical properties can be switched on the fly by taking it from one stable branch to another. In addition, we identified the role played by imperfections and mechanical constraints on the bifurcation diagrams and, ultimately, on the response of the metamaterials.

To guide the design of programmable mechanical materials, in this study we considered a two-dimensional structure of relatively small size and simple geometry. We manually perturbed and physically constrained it to move it between different branches. While this enabled us to demonstrate the power of our approach, real-world applications require systems of arbitrary size and shape and the ability to reprogram the response using remote stimuli. Towards this end, it is important to note that the proposed numerical approach can be readily extended to systems of arbitrary size and shape, which will be likely characterized by markedly different bifurcation diagrams. Moreover, depending on the characteristic size of the structures and on their stiffness, different and remote types of stimuli can be used to move the structure between different branches, including magnetic field [37], heat [38, 39] and swelling [40]. As such, we believe that our strategy enables the design of a new class of reprogrammable mechanical metamaterials.

---

* Corresponding authors: bertoldi@seas.harvard.edu and chr@seas.harvard.edu

[1] M. Kadic, T. Bückmann, R. Schittny, and M. Wegener, Rep. Prog. Phys. **76**, 126501 (2013).

[2] J. Christensen, M. Kadic, O. Kraft, and M. Wegener, MRS Communications **5**, 453 (2015).

[3] K. Bertoldi, V. Vitelli, J. Christensen, and M. van Hecke, Nat. Rev. Mater. **2**, 17066 (2017).

[4] G. N. Greaves, A. L. Greer, R. S. Lakes, and T. Rouxel, Nat. Mater. **10**, 823 (2011).

[5] Q. Wang, J. A. Jackson, Q. Ge, J. B. Hopkins, C. M. Spadaccini, and N. X. Fang, Phys. Rev. Lett. **117**, 175901 (2016).

[6] N. Fang, D. Xi, J. Xu, M. Ambati, W. Srituravanich, C. Sun, and X. Zhang, Nat. Mater. **5**, 452 (2006).

[7] S. A. Cummer, J. Christensen, and A. Alù, Nat. Rev. Mater. **1**, 16001 (2016).

[8] K. Bertoldi, P. M. Reis, S. Willshaw, and T. Mullin, Adv. Mater. **22**, 361 (2010).

[9] S. Babaee, J. Shim, J. C. Weaver, E. R. Chen, N. Patel, and K. Bertoldi, Adv. Mater. **25**, 5044 (2013).

[10] P. Wang, F. Casadei, S. Shan, J. C. Weaver, and K. Bertoldi, Phys. Rev. Lett. **113**, 014301 (2014).

[11] B. Florijn, C. Coulais, and M. van Hecke, Phys. Rev. Lett. **113**, 175503 (2014).

[12] B. Haghpanah, L. Salari-Sharif, P. Pourrajab, J. Hopkins, and L. Valdevit, Adv. Mater. **28**, 8065 (2016).

[13] C. Coulais, A. Sabbadini, F. Vink, and M. van Hecke, Nature **561**, 512 (2018).

[14] R. M. Neville, R. M. J. Groh, A. Pirrera, and M. Schenk, Phys. Rev. Lett. **120**, 254101 (2018).

[15] D. Pihler-Puzović, A. L. Hazel, and T. Mullin, Soft Matter **12**, 7112 (2016).

[16] N. Kidambi, R. L. Harne, and K.-W. Wang, Phys. Rev. E **98**, 043001 (2018).

[17] E. L. Allgower and K. Georg, *Numerical continuation methods: An introduction*, Springer Series in Computational Mathematics (Springer-Verlag, Berlin, 1990).

[18] H. B. Keller, in *Applications of Bifurcation Theory*, edited by P. Rabinowitz (Academic Press, New York, 1977) pp. 359–384.

[19] T. F. C. Chan and H. B. Keller, SIAM J. Sci. Stat. Comput. **3**, 173 (1982).

[20] E. J. Doedel, Congr. Numer. **30**, 265 (1980).

[21] J. Sieber, SIAM J. Appl. Dyn. Syst. **1**, 248 (2002).

[22] D. M. Ambrose and J. Wilkening, Comm. App. Math. and Comp. Sci. **4**, 177 (2009).

[23] J. Wilkening, Phys. Rev. Lett. **107**, 184501 (2011).

[24] C. H. Rycroft and J. Wilkening, J. Comput. Phys. **255**, 612 (2013).

[25] C. G. Johnson, U. Jain, A. L. Hazel, D. Pihler-Puzovic, and T. Mullin, Proceedings of the Royal Society A: mathematical, physical and engineering sciences **473**, urn:issn:1364 (2017).

[26] A. Logg, K. A. Mardal, G. N. Wells, *et al.*, *Automated Solution of Differential Equations by the Finite Element Method* (Springer, 2012).

[27] P. E. Farrell, C. H. L. Beentjes, and A. Birkisson, arXiv:1603.00809 [math.NA] (2016).

[28] P. E. Farrell, A. Birkisson, and S. W. Funke, SIAM Journal on Scientific Computing **37**, A2026 (2015).

[29] R. Ogden, *Non-linear Elastic Deformations*, Dover Civil and Mechanical Engineering (Dover Publications, 1997).

[30] T. Mullin, S. Deschanel, K. Bertoldi, and M. C. Boyce, Phys. Rev. Lett. **99**, 084301 (2007).

[31] Y. Zhang, E. A. Matsumoto, A. Peter, P.-C. Lin, R. D. Kamien, and S. Yang, Nano Lett. **8**, 1192 (2008).

[32] C. Coulais, C. Kettenis, and M. van Hecke, Nat. Phys. **14**, 40 (2017).

[33] See Supplemental Material at [URL] for additional numerical results, details on experiments and fabrication, plus information on data and code availability.

[34] M. Golubitsky, I. Stewart, and D. Schaeffer, *Singularities and Groups in Bifurcation Theory: Volume II*, Applied Mathematical Sciences, Vol. 69 (Springer, 1988).

[35] G. Wu, Y. Cho, I. Choi, D. Ge, J. Li, H. N. Han, T. Lubensky, and S. Yang, Adv. Mater. **27**, 2747 (2015).

[36] S. Janbaz, F. S. L. Bobbert, M. J. Mirzaali, and A. A. Zadpoor, Mater. Horiz. **6**, 1138 (2019).

[37] Y. Kim, H. Yuk, R. Zhao, S. A. Chester, and X. Zhao, Nature **558**, 274 (2018).

[38] T. G. Leong, C. L. Randall, B. R. Benson, N. Bassik, G. M. Stern, and D. H. Gracias, Proc. Natl. Acad. Sci. **106**, 703 (2009).

[39] Y. Liu, J. K. Boyles, J. Genzer, and M. D. Dickey, Soft Matter **8**, 1764 (2012).

[40] J. Kim, J. A. Hanna, M. Byun, C. D. Santangelo, and R. C. Hayward, Science **335**, 1201 (2012).